

ARTICLE

<https://doi.org/10.1038/s42003-019-0482-7>

OPEN

Crystal structure of human endothelin ET_B receptor in complex with peptide inverse agonist IRL2500

Chisae Nagiri^{1,3}, Wataru Shihoya^{1,3}, Asuka Inoue², Francois Marie Ngako Kadji², Junken Aoki² & Osamu Nureki¹

Endothelin receptors (ET_A and ET_B) are G-protein-coupled receptors activated by endothelin-1 and are involved in blood pressure regulation. IRL2500 is a peptide-mimetic of the C-terminal tripeptide of endothelin-1, and has been characterized as a potent ET_B-selective antagonist, which has preventive effects against brain edema. Here, we report the crystal structure of the human ET_B receptor in complex with IRL2500 at 2.7 Å-resolution. The structure revealed the different binding modes between IRL2500 and endothelin-1, and provides structural insights into its ET_B-selectivity. Notably, the biphenyl group of IRL2500 penetrates into the transmembrane core proximal to D^{2.50}, thus stabilizing the inactive conformation. Using the newly-established constitutively active mutant, we clearly demonstrate that IRL2500 functions as an inverse agonist for the ET_B receptor. The current findings will expand the chemical space of ETR antagonists and facilitate the design of inverse agonists for other class A GPCRs.

¹Department of Biological Sciences, Graduate School of Science, The University of Tokyo, Bunkyo-ku, Tokyo 113-0033, Japan. ²Graduate School of Pharmaceutical Sciences, Tohoku University, 6-3, Aoba, Aramaki, Aoba-ku, Sendai 980-8578 Miyagi, Japan. ³These authors contributed equally: Chisae Nagiri, Wataru Shihoya. Correspondence and requests for materials should be addressed to W.S. (email: wtrshh9@gmail.com) or to O.N. (email: nureki@bs.s.u-tokyo.ac.jp)

Endothelin receptors (ETRs) are G-protein-coupled receptors (GPCR) activated by vasoactive peptide, endothelins¹. Two ETR subtypes (ET_A and ET_B) are widely expressed in the vascular endothelium, brain, and other circulatory organs^{2,3}. Endothelin-1 (ET-1) activates the both ETRs with sub-nanomolar affinities. The activation of the ET_A receptor leads to potent and long-lasting vasoconstriction, whereas that of the ET_B receptor induces nitric oxide-mediated vasorelaxation. Therefore, the up-regulation of ET-1 is related to circulatory-system diseases, including pulmonary arterial hypertension (PAH)^{4–7}. Moreover, the autocrine and paracrine signaling functions of ET-1 through the ET_A receptor play a critical role in tumor growth and survival⁸. Thus, ETR antagonists have been developed for the treatment of circulatory-system diseases and cancers^{6,7}. Bosentan is the first orally-active ETR antagonist^{9,10}, and is used to treat PAH. The ET_B receptor is the prominent ETR subtype in the brain, with high expression levels in astrocytes¹¹. Stimulation of the ET_B receptor modulates astrocytic responses, indicating its important roles in regulating astrocytic functions¹². The up-regulation of the astrocytic ET_B receptor by ET-1 increases the vascular permeability and reduces the AQP4 levels, thereby aggravating vasogenic brain edema¹¹. The application of ET_B-selective antagonists may provide preventive effects against brain edema in the acute phase of brain insults^{13–16}.

To date, most ETR antagonists have been developed based on bosentan^{17,18}. The ETR antagonists that have been developed till now are mostly N-heterocyclic sulfonamides with similar structures and molecular weights, and non-sulfonamide antagonists (atrasentan, ambrisentan, darusentan, and enrasentan) still retain high similarities with each other and with the sulfonamides⁶. Since the ETR antagonists are chemically very similar⁷, and the expanded chemical space should be exploited. IRL2500 is a peptide-mimetic ETR antagonist developed based on the partial region of ET-1¹⁹, not on bosentan. IRL2500 has been characterized as an ET_B-selective antagonist with an IC₅₀ value of 1.2 nM²⁰, which shows higher affinity than that of bosentan. In an animal model, the intracerebroventricular administration of IRL2500 attenuated the cold injury-mediated brain edema and disruption of the blood–brain barrier, indicating the neuroprotective effect of IRL2500^{14,15}. Clarification of the IRL2500 binding mode would facilitate the expansion of the chemical space of ET agents.

We previously reported the crystal structures of the ET_B receptor bound to ET-1²¹ and bosentan²²; however, both the binding mode and ET_B-selectivity of IRL2500 remained to be elucidated. Here, we present the crystal structure of the ET_B receptor in complex with IRL2500. This structure revealed the unique binding mode of IRL2500, which differs from those of ET-1 and bosentan. Structure-guided functional analyses clearly demonstrate that IRL2500 functions as an inverse agonist for the ET_B receptor, and thus will provide the basis for the design of inverse agonists for other class A GPCRs.

Results

Overall structure. For crystallization, we used the previously established, thermostabilized ET_B receptor (ET_B-Y4)^{22,23}. The IC₅₀ value of IRL2500 for ET_B-Y4 was similar to that for the wild type receptor in the TGF α shedding assay²⁴ (Fig. 1a), suggesting that the thermostabilizing mutations minimally affect the IRL2500 binding. In contrast, the IC₅₀ value of IRL2500 for the ET_A receptor is over 3 μ M (Fig. 1a), indicating that IRL2500 has over 100-fold ET_B-selectivity, consistent with the previous pharmacological analysis²⁰. To facilitate crystallization, we replaced the third intracellular loop (ICL3) of the receptor with minimal T4 Lysozyme²⁵ (ET_B-Y4-mT4L). Using in meso crystallization²⁶,

we obtained crystals of ET_B-Y4-mT4L in complex with IRL2500 (Supplementary Fig. 1a, b). In total, 58 datasets were collected and merged by the data processing system KAMO²⁷. Eventually, we determined the ET_B structure in complex with IRL2500 at 2.7 Å resolution, by molecular replacement using the antagonist-bound ET_B structure (PDB code: 5X93) (Table 1).

The overall structure consists of the canonical 7 transmembrane helices (TM), the amphipathic helix 8 at the C-terminus (H8), and two antiparallel β -strands in the extracellular loop 2 (ECL2), as in the previously determined ET_B structures (Fig. 1b). The IRL2500-bound structure is similar to the bosentan-bound structure, rather than the ET-1-bound structure (R.M.S.D. values for Ca atoms = 1.34 and 1.95 Å, respectively), reflecting the inactive conformation. We observed a remarkable difference in the conformation of ECL2. The β strands are opened up by 9 Å, as compared with those in the ligand-free structure (Fig. 1c and Supplementary Fig. 2a), and are the widest among the peptide-activated class A GPCRs (Supplementary Fig. 2b). This conformation is facilitated by the crystal packing (Supplementary Fig. 2c), and is not a consequence of IRL2500 binding. This structural feature indicates the ECL2 is highly flexible in the inactive conformation of the ET_B receptor, to capture the large peptide ligand endothelin.

IRL2500 binding site. We first describe the IRL2500 binding mode. IRL2500 consists of a tryptophan, a biphenyl group and a 3,5-dimethylbenzoyl group¹⁹. The biphenyl group forms a peptide bond with the tryptophan, and a peptoid bond with the dimethylbenzoyl group (Fig. 1d). IRL2500 binds to the transmembrane binding cleft exposed to the extracellular side, with a clear electron density (Supplementary Fig. 3a, b). The carboxylate group of the tryptophan moiety in IRL2500 forms salt bridges with R343^{6,55} (superscripts indicate Ballesteros–Weinstein numbers²⁸) (Fig. 1e, f). The tryptophan side chain of IRL2500 forms a hydrogen bond with the carbonyl group of the N158^{2,61} side chain and a cation– π interaction with the K161^{2,64} side chain. The tryptophan also forms extensive van der Waals interactions with V177^{3,28}, P178^{3,29}, and F240^{4,64}. The dimethylbenzoyl group of IRL2500 forms van der Waals interactions with the hydrophobic pocket, and is surrounded by V185^{3,36}, L277^{5,42}, Y281^{5,46}, W336^{6,48} and L339^{6,51}. The biphenyl group penetrates deeply into the receptor core proximal to D147^{2,50}, and forms van der Waals interactions with D147^{2,50}, H150^{2,53}, W336^{6,48}, and S376^{7,43}. Overall, the carboxylate of IRL2500 is specifically recognized by the positively charged residues of the ET_B receptor, and the other moieties fill the space within the transmembrane binding pocket.

To elucidate the structural basis for the ET_B-selectivity of IRL2500, we compared the residues constituting the IRL2500 binding site between the ET_B and ET_A receptors (Fig. 2a and Supplementary Fig. 4). Most of the residues are conserved, while H150^{2,53}, V177^{3,28}, and S376^{7,43} are substituted for the bulkier residues Y129^{2,53}, F161^{3,28}, and T359^{7,43} in the ET_A receptor, respectively. These substitutions may cause steric clashes with the aromatic groups of IRL2500 and reduce its affinity. To investigate this hypothesis, we measured the IC₅₀ values of IRL2500 for the H150Y, V177F, and S376T ET_B receptor mutants. These mutants showed similar responses for ET-1 in the TGF α shedding assay (Supplementary Fig. 5a). The H150Y mutant showed a similar response for IRL2500, and the S376T mutant showed a 3-fold increased potency (that is, 3-fold smaller IC₅₀ value) of IRL2500. Only V177F showed a 6-fold decreased potency of IRL2500 (Fig. 2b and Table 2), suggesting that the F161^{3,28} in the ET_A receptor sterically clashes with the tryptophan moiety of IRL2500. Moreover, the H150Y/V177F double mutant showed the further

Table 1 Data collection and refinement statistics

	IRL2500-ET _B
Data collection	
Space group	I422
Cell dimensions	
<i>a</i> , <i>b</i> , <i>c</i> (Å)	110.0, 110.0, 291.7
α , β , γ (°)	90, 90, 90
Resolution (Å) ^a	43.88–2.70 (2.797–2.70)
<i>R</i> _{meas} ^a	0.295 (3.946)
($\langle I/\sigma(I) \rangle$) ^a	10.74 (1.08)
CC _{1/2} ^a	0.995 (0.798)
Completeness (%) ^a	99.66 (99.35)
Redundancy ^a	19.3 (19.6)
Refinement	
Resolution (Å)	43.88–2.70
No. reflections	25,069
<i>R</i> _{work} / <i>R</i> _{free}	0.2216/0.2653
No. atoms	
Protein	3258
Ligand	43
Water/ion/lipid	240
Averaged <i>B</i> -factors (Å ²)	
Protein	83.41
Ligand	51.4
Water/ion/lipid	94.45
R.M.S. deviations from ideal	
Bond lengths (Å)	0.003
Bond angles (°)	0.65
Ramachandran plot	
Favored (%)	99.26
Allowed (%)	0.74
Outlier (%)	0

^aValues in parentheses are for highest-resolution shell

to the ET_B receptor. In addition, like bosentan, the aromatic moieties of IRL2500 fit within the local hydrophobic pockets in the ET_B receptor. Overall, IRL2500 has moieties that form similar binding interactions to those of bosentan. However, bosentan lacks the moiety corresponding to the biphenyl group of IRL2500, which deeply penetrates into the receptor core (Fig. 3f). Thus, IRL2500 fits into the pocket more tightly as compared with bosentan, contributing to its higher affinity for the ET_B receptor.

IRL2500 functions as an inverse agonist. To obtain mechanistic insights into the receptor inactivation by IRL2500, we compared the ET_B structures bound to ET-1, bosentan, and IRL2500. Previous structural studies showed that ET-1 binding induces the inward motion of the extracellular portion of TM6 including W336^{6,48}, leading to receptor activation on the intracellular side²¹ (Fig. 4a). Bosentan binding sterically prevents the inward motion of W336^{6,48} with its 2-methoxyphenoxy group, and thus functions as an antagonist²² (Fig. 4b). The dimethylbenzoyl group of IRL2500 superimposes well with the 2-methoxyphenoxy group of bosentan and similarly prevents the inward motion (Fig. 4b). Moreover, the dimethylbenzoyl and biphenyl groups of IRL2500 sandwich the W336^{6,48} side chain, tightly preventing its inward rotation (Fig. 4c). These observations suggest that IRL2500 tightly prevents the transition to the active state, as compared with bosentan, thereby possibly working as an inverse agonist that reduces the basal activity.

To investigate the inverse agonist activity of IRL2500 for the ET_B receptor, we first measured the ligand-induced AP-TGF α release responses. In the wild-type ET_B, treatment with IRL2500 or the antagonist bosentan with the cells for 4 h-incubation did not change the receptor activation level (Fig. 4d and Table 3).

These data suggested that IRL2500 either does not have the inverse agonist activity or that the assay is not sensitive enough to detect the inverse agonist activity. Indeed, we observed that the basal activity of the ET_B receptor was very low in the assay and thus we could not distinguish whether IRL2500 functions as an antagonist or an inverse agonist by this assay.

Therefore, we tried the same assay by utilizing a mutation to facilitate the constitutive activity of the ET_B receptor. Constitutively active mutant GPCRs have been employed in pharmacological characterizations of inverse agonists³⁰, because such mutant GPCRs allow the signal measurement in a larger detection window. The substitution of the highly conserved L^{3,43} to glutamine has been identified as a causative activating mutation in the *TSHR*³¹ and *CYSLTR2*³² genes, which are related to hyperthyroidism and uveal melanoma, respectively. Therefore, we transferred the L^{3,43}Q mutation into the ET_B receptor (ET_B-L192^{3,43}Q) and examined its constitutive activity. We found that ET_B-L^{3,43}Q induced spontaneous AP-TGF α release (Fig. 4e), indicating that L^{3,43}Q functions as a constitutively active mutation in the ET_B receptor. We confirmed that this mutation also increased the constitutive activity in the ET_A receptor (Supplementary Fig. 6a). The L^{3,43}Q-mutant ET_B and ET_A increased the potency of both ET-1 (EC₅₀) and the antagonists (IC₅₀) by approximately 5-fold and 2-fold, respectively (Supplementary Fig. 5b–d). We evaluated the inverse agonist activities of these compounds, using the constitutively active mutant, ET_B-L^{3,43}Q (Fig. 4f and Table 3). As expected, the antagonist bosentan did not change the receptor activation from the baseline level. Conversely, IRL2500 reduced the basal activity of the ET_B-L^{3,43}Q mutant (EC₅₀ = 0.92 nM). Both bosentan and IRL2500 did not change the basal activity of the ET_A-L^{3,43}Q (Supplementary Fig. 6b, c). These data indicate that IRL2500 functions as a potent inverse agonist for the ET_B receptor, consistent with the structural observations. The biphenyl group of IRL2500 prevents the inward motion of W336^{6,48} to stabilize the inactive conformation, and thus IRL2500 functions as an inverse agonist.

In addition to IRL2500, K-8794 and BQ-788 have been characterized as potent ET_B-selective antagonists. K-8794 is a high-affinity analog of bosentan²², whereas BQ-788 is a peptide analog with distinct chemical moieties, as compared with those of IRL2500 and bosentan³³. We investigated the inverse agonist activities of K-8794 and BQ-788, using the constitutively active mutants of the ETRs (Fig. 4f and Table 3). K-8794 and BQ-788 reduced the basal activity of the ET_B-L^{3,43}Q with EC₅₀ values of 0.61 and 0.96 nM, respectively, indicating that they also function as inverse agonists. K-8794 and BQ-788 showed higher and lower efficacies (*E*_{max}) of the inverse agonist activity than that of IRL2500, respectively. The K-8794-bound ET_B structure has been determined and thus we compare the ET_B structures bound to K-8794, bosentan, and IRL2500. The chemical structure of K-8794 is similar to that of bosentan, but K-8794 has a dimethylphenyl group linked to the peptide bond. This modification slightly displaces the overall position of K-8794, thereby moving W336^{6,48} outward by the interactions with the 6-methoxyphenoxy and the alkyl groups (Supplementary Fig. 7a). Therefore, K-8794 tightly prevents the inward rotation of W336^{6,48}, in a similar manner to IRL2500 (Supplementary Fig. 7b). We thus suggest that this structural feature likely contributes to the inverse agonist activity of K-8794.

Discussion

We have determined the crystal structure of the ET_B receptor in complex with the peptide-mimetic drug IRL2500, and thus elucidated the detailed receptor interactions and the structural basis for its ET_B selectivity. Although IRL2500 is designed to mimic the

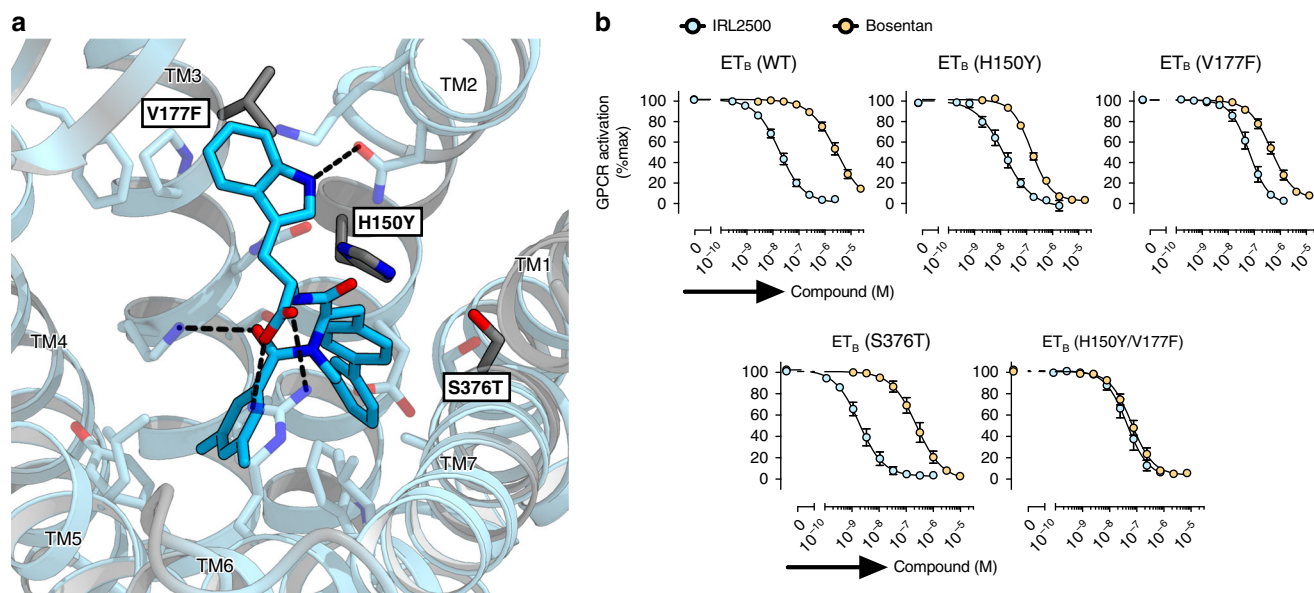


Fig. 2 Conservation of the IRL2500 binding site. **a** Sequence conservation of the IRL2500 binding site between ET_A and ET_B , mapped onto the IRL2500-bound structure. Conserved and non-conserved residues are colored sky blue and gray, respectively. The receptor residues involved in IRL2500 binding are shown as sticks. The dashed lines show hydrogen bonds. **b** Effects of IRL2500 and bosentan on the ET-1 (0.5 nM)-induced release of AP-TGF α in HEK293 cells expressing the mutant ET_B receptors. For each experiment, the AP-TGF α release response in the absence of IRL2500 is set at 100%. Data are displayed as means \pm SEM (standard error of the mean) from four to six independent experiments

Table 2 Pharmacological characterization of mutant ET_B receptors

		ET_B -WT	H150Y	V177F	S376T	H150/V177F
<i>n</i>		6	4	4	4	4
ET-1	EC ₅₀ (nM)	0.14	0.090	0.093	0.16	0.11
	pEC ₅₀ (mean \pm SEM)	9.85 \pm 0.07	10.05 \pm 0.10	10.03 \pm 0.11	9.79 \pm 0.04	9.97 \pm 0.08
IRL2500	IC ₅₀ (nM)	21	18	130	6.1	180
	pIC ₅₀ (mean \pm SEM)	7.67 \pm 0.09	7.74 \pm 0.15	6.87 \pm 0.13	8.22 \pm 0.15	6.75 \pm 0.15
	K _B (nM)	2.4	0.78	7.8	0.63	12
	pK _B (mean \pm SEM)	8.62 \pm 0.07	9.11 \pm 0.12	8.11 \pm 0.07	9.20 \pm 0.08	7.93 \pm 0.14
	ΔK_B	1	3.0	0.30	4.0	0.20
Bosentan	ΔpK_B (mean \pm SEM)	0	0.47 \pm 0.11	-0.53 \pm 0.06	0.60 \pm 0.03	-0.70 \pm 0.14
	IC ₅₀ (nM)	3,300	270	1100	680	270
	pIC ₅₀ (mean \pm SEM)	5.48 \pm 0.11	6.57 \pm 0.05	5.97 \pm 0.11	6.17 \pm 0.16	6.56 \pm 0.11
	K _B (nM)	400	12	70	71	17
	pK _B (mean \pm SEM)	6.39 \pm 0.09	7.92 \pm 0.13	7.16 \pm 0.05	7.15 \pm 0.10	7.78 \pm 0.02
	ΔK_B	1	35	6.1	5.8	26
	ΔpK_B (mean \pm SEM)	0	1.55 \pm 0.12	0.79 \pm 0.08	0.76 \pm 0.11	1.41 \pm 0.06

partial region of ET-1, its binding mode is quite different. Moreover, using the constitutively active mutant ET_B -L^{3,43}Q, we revealed that IRL2500 together with K-8794 and BQ-788, but not bosentan, function as a potent inverse agonist for the ET_B receptor, and provided the structural basis for their inverse agonist activities. Our study sheds light on the new aspects of the ET_B -selective antagonists, and deepens our understanding of ETR pharmacology.

Although small-molecule ETR antagonists have been developed over the years; however, most ETR antagonists have been designed based on bosentan. Thus, the presently available ETR antagonists are chemically very similar. IRL2500 was developed based on ET-1 and has totally distinct chemical moieties, as compared with those of bosentan. However, the comparison of the IRL2500 and bosentan binding modes revealed the unexpected similarity in their binding interactions. This observation

suggests that the charge-complementary interactions in the center of the pocket form the core of the receptor-antagonist interactions, and the other aromatic moieties fit the local hydrophobic pocket. The ligand binding pocket in the inactive ET_B structures is larger than those in other GPCR structures, and thus aromatic moieties may be necessary to fit well within the pocket.

Our study revealed that the biphenyl group of IRL2500 penetrates deeply into the receptor core proximal to D1472⁵⁰, preventing the inward motion of W336^{6,48} in TM6, and thus IRL2500 functions as an inverse agonist (Fig. 5a, b). The deep binding modes of the inverse agonists are also observed in the 5-HT_{2C}R and BLT1 structures (Fig. 5c-f). In the 5-HT_{2C}R structure, the 4-fluorophenyl group of the inverse agonist ritanserin interacts with F320^{6,44} and W324^{6,48}, the purported “toggle switch” important for GPCR activation³⁴ (Fig. 5c, d). In the BLT1 structure, the benzamidine group of the inverse agonist

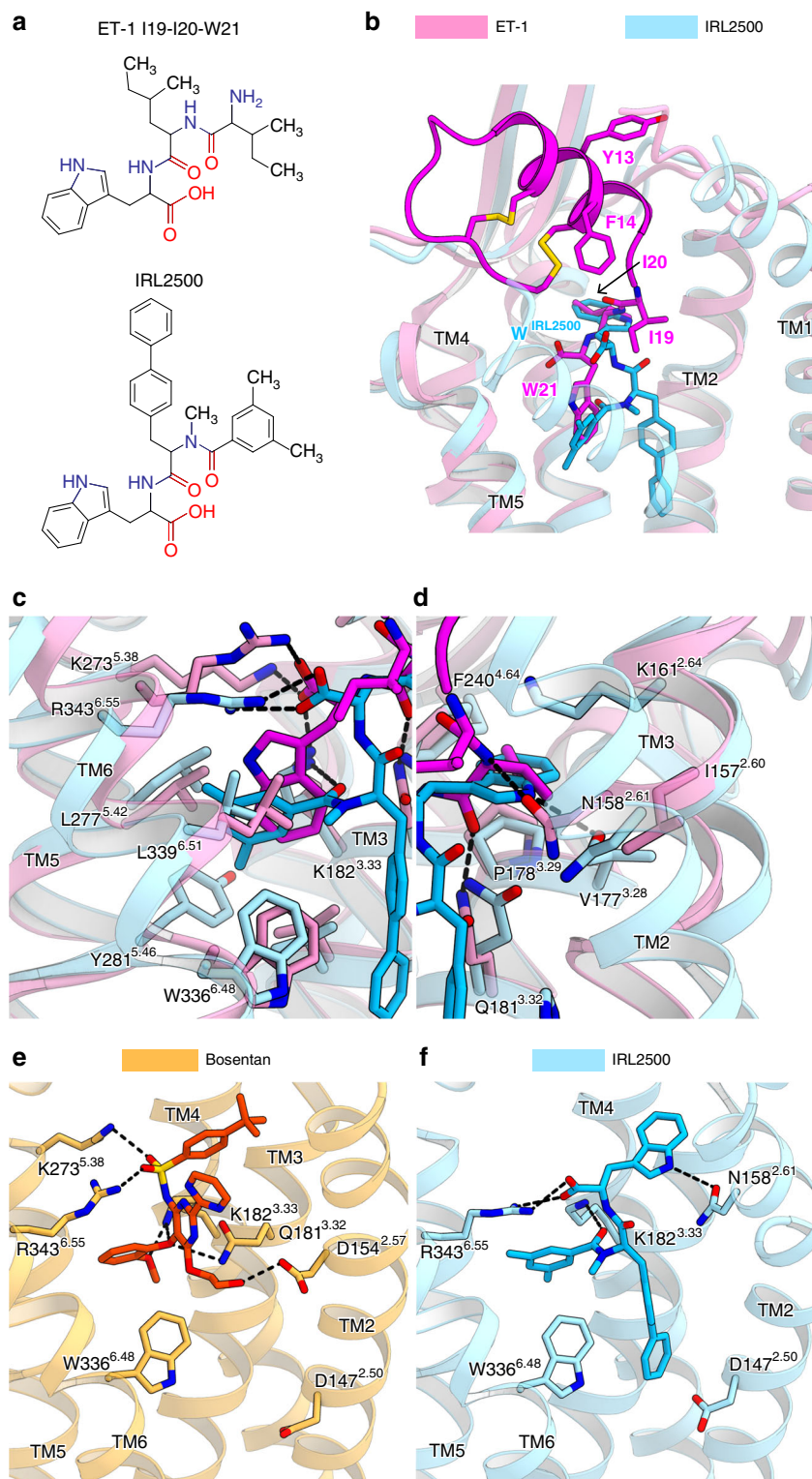


Fig. 3 Comparison of binding modes of IRL2500, ET-1, and bosentan. **a** Chemical structures of IRL2500 and the C-terminal tripeptide of ET-1. **b** Superimposition of the IRL2500- and ET-1-bound ET_B receptors (PDB code: 5GLH). The ET-1- and IRL2500-bound receptors are shown as pink and sky blue ribbons, respectively. IRL2500 is shown as a stick model. ET-1 is shown as a magenta ribbon with stick models of the peptide residues (Y13, F14, I19, I20, and W21). **c, d** The residues interacting with both IRL2500 and ET-1 are shown as sticks. **e, f** Binding pockets for bosentan (**e**) and IRL2500 (**f**), viewed from the membrane plane. The bosentan-bound receptor (PDB code: 5XPR) is shown as a thin orange ribbon model. The residues involved in bosentan binding (D154^{2.57}, Q181^{3.32}, K182^{3.33}, K273^{5.38}, W336^{6.48} and R343^{6.55}) and D147^{2.50} are shown as sticks. Bosentan is shown as an orange stick model. IRL2500 and the IRL2500-bound receptor are colored as in panel (**a**). The residues involved in IRL2500 binding (N158^{2.61}, K182^{3.33}, R343^{6.55}, D147^{2.50} and W336^{6.48}) are shown as sticks

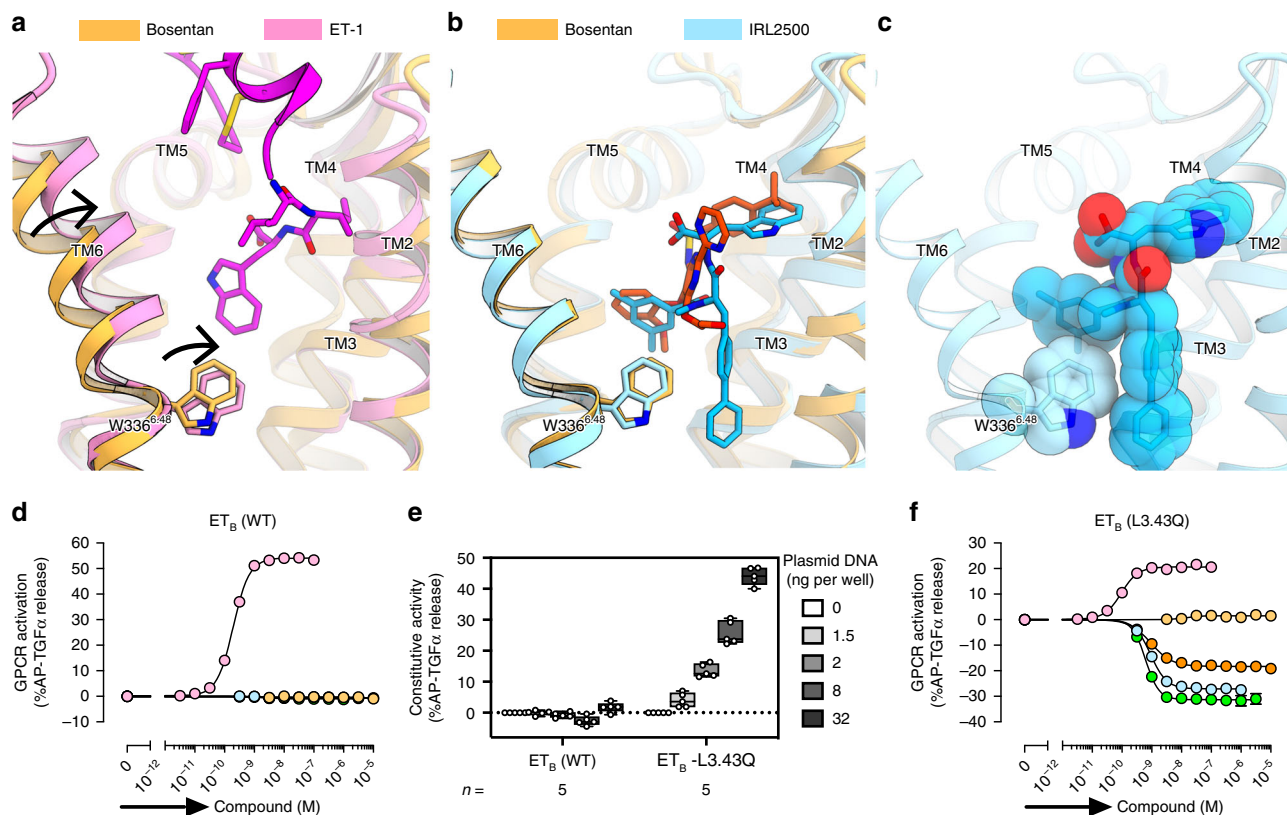


Fig. 4 Inverse agonist activity of IRL2500. **a, b** Structural changes upon ET-1 and IRL2500 binding, as compared with the bosentan-bound structure, colored as in Fig. 3. Black arrows indicate the inward movements of TM6 and W336^{6,48}. **c** CPK representations of IRL2500 and the W336^{6,48} side chain. **d** Effects of ET-1 and the ET_B antagonists (bosentan, IRL2500, K-8794, and BQ-788) on the AP-TGFα release for the ET_B receptor. For each experiment, the spontaneous AP-TGFα release response in the absence of the compound is set at the baseline. Data are displayed as means ± SEM from six to eleven independent experiments. **e** Constitutive activity of the L192^{3,43}Q-mutant ET_B receptor (ET_B-L^{3,43}Q). HEK293 cells were transfected with titrated volumes of a plasmid encoding the wild-type ET_B (ET_B-WT) or the L^{3,43}Q-mutant ET_B (ET_B-L^{3,43}Q) and accumulated AP-TGFα release during 24 h after transfection was measured. The AP-TGFα release signal in the 0 ng receptor plasmid was set as the baseline. Data are displayed as a box-and-whisker plot from five independent experiments with each performed in 4–6 replicates. **f** Effects of ET-1 and the ET_B antagonists (bosentan, IRL2500, K-8794 and BQ-788) on the AP-TGFα release for the constitutively active ET_B receptor (ET_B-L^{3,43}Q). For each experiment, the spontaneous AP-TGFα release response in the absence of the compound is set at the baseline. Data are displayed as means ± SEM from seven to twelve independent experiments. In the inverse agonist experiments (**d, f**), the cells were incubated with a test compound for 4 h

Table 3 Characterization of inverse agonist activities of endothelin receptor antagonists

	ET _B -WT	ET _B -L192 ^{3,43} Q
ET-1		
EC ₅₀ (nM)	0.19	0.094
pEC ₅₀ (mean ± SEM)	9.72 ± 0.03	10.03 ± 0.04
E _{max} ± SEM	53.6 ± 1.7	20.5 ± 1.3
n	10	12
Bosentan		
EC ₅₀ (nM)	NA	NA
pEC ₅₀ (mean ± SEM)	NA	NA
E _{max} ± SEM	<2%	<2%
n	11	12
IRL2500		
EC ₅₀ (nM)	NA	0.92
pEC ₅₀ (mean ± SEM)	NA	9.03 ± 0.05
E _{max} ± SEM	<2%	-27.0 ± 1.1
n	11	12
K-8794		
EC ₅₀ (nM)	NA	0.61
pEC ₅₀ (mean ± SEM)	NA	9.21 ± 0.04
E _{max} ± SEM	<2%	-31.5 ± 2.0
n	6	7
BQ-788		
EC ₅₀ (nM)	NA	0.96
pEC ₅₀ (mean ± SEM)	NA	9.02 ± 0.03
E _{max} ± SEM	<2%	-18.5 ± 0.7
n	6	7

BIIL260 fits into a sodium binding pocket around D147^{2,50} (Fig. 5e, f), which is highly conserved among the class A GPCRs³⁵. Sodium selectively competes with agonist binding in most class A GPCRs by stabilizing the inactive conformations, and the sodium binding site is thus an important pocket targeted in the design of negative allosteric modulators and inverse agonists. Instead of the sodium, the benzamidine group of BIIL260 directly hydrogen bonds with D^{2,50}, similarly stabilizing the inactive conformation³⁶ (Fig. 5f). The binding mode of IRL2500 is similar to that of BIIL260 in BLT1, rather than that of ritanserlin in the 5-HT_{2c}R (Fig. 5g, h). Although the biphenyl group of IRL2500 does not form any hydrogen-bonding interactions with the receptor, it prevents the conformational change around the D2.50 in a similar manner to the benzamidine moiety of BIIL260 (Fig. 5b, f). For the design of effective inverse agonists, the biphenyl moiety would also be useful as a modulation part along with another moiety that exerts specific and tight binding to the orthosteric site, as well as a benzamidine group.

Methods

Expression and purification. The haemagglutinin signal peptide, followed by the Flag epitope tag (DYKDDDDK) and a nine-amino-acid linker, was added to the N-terminus of the receptor, and a tobacco etch virus (TEV) protease recognition

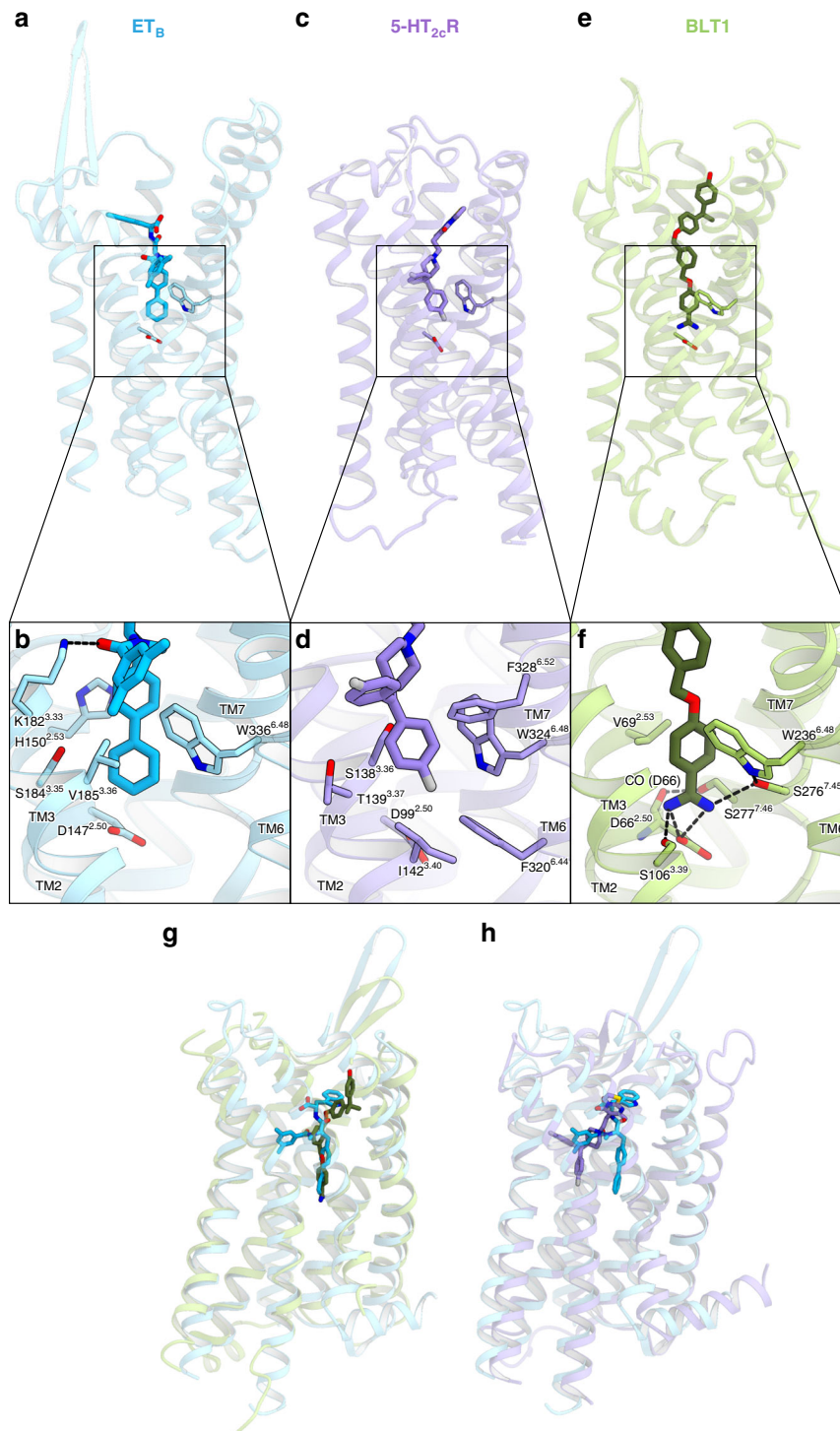


Fig. 5 Structural comparison with the inverse agonist-bound GPCR structures. **a–f** The structures of the IRL2500-bound ET_B receptor (**a, b**), Ritanserin-bound 5-HT_{2c}R (PDB code: 6BQH) (**c, d**), and the BIIL260-bound BLT1 (PDB code: 5X33) (**e, f**), shown as sky blue, purple and light green ribbons, respectively. The inverse agonists IRL2500, ritanserin, and BIIL260 are shown as sticks. The binding interactions around the sodium binding site are shown in (**b**), (**d**), and (**f**). The residues involved in ligand binding are represented with sticks. Hydrogen bonds are indicated by black dashed lines. In the IRL2500-bound ET_B structure, the biphenyl group of IRL2500 forms van der Waals interactions with the receptor, and does not form any hydrogen-binding interactions. In the BIIL260-bound BLT1 structure, BIIL260 forms hydrogen bonds with D66^{2.50}, S106^{3.39} and S276^{7.45}. **g, h** Superimposition of the IRL2500-bound ET_B structure with the BLT1 (**g**) and 5-HT_{2c}R (**h**) structures

sequence was introduced between G57 and L66, to remove the disordered N-terminus during the purification process. The C-terminus was truncated after S407, and three cysteine residues were mutated to alanine (C396A, C400A, and C405A) to avoid heterogeneous palmitoylation. To improve crystallogenes, we introduced four thermostabilizing mutations (R124Y^{1.55}, K270A^{5.35}, S342A^{6.54}, and I381A^{7.48})

and inserted minimal T4 lysozyme²⁵ into intracellular loop 3, between K303^{5.68} and L311^{6.23} (ET_B-Y4-mT4L²²).

The thermostabilized construct ET_B-Y4-mT4L was subcloned into a modified pFastBac vector, with the resulting construct encoding a TEV cleavage site followed by a GFP-His¹⁰ tag at the C-terminus. The recombinant baculovirus was prepared

using the Bac-to-Bac baculovirus expression system (Invitrogen). Sf9 insect cells were infected with the virus at a cell density of 4.0×10^6 cells per ml in Sf900 II medium, and grown for 48 h at 27 °C. The harvested cells were disrupted by sonication, in buffer containing 20 mM Tris-HCl, pH 7.5, and 20% glycerol. The crude membrane fraction was collected by ultracentrifugation at 180,000 g for 1 h. The membrane fraction was solubilized in buffer, containing 20 mM Tris-HCl, pH 7.5, 200 mM NaCl, 1% DDM, 0.2% cholesterol hemisuccinate, 10 μ M IRL2500, and 2 mg ml⁻¹ iodoacetamide, for 1 h at 4 °C. The supernatant was separated from the insoluble material by ultracentrifugation at 180,000 g for 20 min, and incubated with TALON resin (Clontech) for 30 min. The resin was washed with ten column volumes of buffer, containing 20 mM Tris-HCl, pH 7.5, 500 mM NaCl, 0.1% LMNG, 0.01% CHS, 10 μ M IRL2500, and 15 mM imidazole. The receptor was eluted in buffer, containing 20 mM Tris-HCl, pH 7.5, 500 mM NaCl, 0.01% LMNG, 0.001% CHS, 10 μ M IRL2500, and 200 mM imidazole. The eluate was treated with TEV protease and dialyzed against buffer (20 mM Tris-HCl, pH 7.5, 500 mM NaCl, and 10 μ M IRL2500). The cleaved GFP-His₁₀ tag and the TEV protease were removed with Co²⁺-NTA resin. The receptor was concentrated and loaded onto a Superdex200 10/300 Increase size-exclusion column, equilibrated in buffer containing 20 mM Tris-HCl, pH 7.5, 150 mM NaCl, 0.01% LMNG, 0.001% CHS, and 10 μ M IRL2500. Peak fractions were pooled, concentrated to 40 mg ml⁻¹ using a centrifugal filter device (Millipore 50 kDa MW cutoff), and frozen until crystallization. During the concentration, IRL2500 was added to a final concentration of 100 μ M.

Crystallization. The purified receptor was reconstituted into molten lipid (monoolein and cholesterol 10:1 by mass) at a weight ratio of 1:1.5 (protein:lipid)³⁷. The protein-laden mesophase was dispensed into 96-well glass plates in 30 nl drops and overlaid with 800 nl precipitant solution by a Gryphon LCP robot (Art Robbins Instruments)²⁶. Crystals of ET_B-Y4-mT4L bound to IRL2500 were grown at 20 °C in precipitant conditions containing 30% PEG300, 100 mM Bis-tris, pH 7.5, 150 mM sodium phosphate monobasic, and 10 mM TCEP hydrochloride. The crystals were harvested directly from the LCP using micromounts (MiTeGen) or LithoLoops (Protein Wave) and frozen in liquid nitrogen, without adding any extra cryoprotectant.

Data collection and structure determination. X-ray diffraction data were collected at the SPring-8 beamline BL32XU, with $10 \times 15 \mu\text{m}^2$ (width \times height) micro-focused beams and an EIGER X 9M detector (Dectris). Various wedge data sets (10°) per crystal were mainly collected with the ZOO system³⁸, an automatic data-collection system developed at SPring-8. The loop-harvested microcrystals were identified by raster scanning and subsequently analyzed by SHIKA³⁹. The collected images were automatically processed with KAMO⁴⁰ (<https://github.com/keitaroyam/yamtbx>). Each data set was indexed and integrated with XDS⁴¹, and the datasets were hierarchically clustered by using the correlation coefficients of the intensities between datasets⁴¹. After the rejection of outliers, 58 data sets were finally merged with XSCALE⁴¹. The IRL2500-bound structure was determined by molecular replacement with PHASER⁴², using the K-8794-bound ET_B structure (PDB code: 5X93). Subsequently, the model was rebuilt and refined using COOT⁴³ and PHENIX⁴⁴, respectively. The final model of IRL2500-bound ET_B-Y4-T4L contained residues 91-207, 214-303, and 311-403 of ET_B, 1-11 and 19-117 of mT4L, IRL2500, 8 monoolein molecules, 4 phosphoric acids, and 34 water molecules. The model quality was assessed by MolProbity⁴⁵. Figures were prepared using CueMol (<http://www.cuemol.org/ja/>).

TGF α shedding assay. The TGF α shedding assay, which measures the activation of G_{q/11} and G_{12/13} signaling²⁴, was performed as described previously²². Briefly, a plasmid encoding an ET_B construct with an internal FLAG epitope tag or an ET_A construct was transfected, together with a plasmid encoding alkaline phosphatase (AP)-tagged TGF α (AP-TGF α), into HEK293A cells by using a polyethylenimine (PEI) transfection reagent (1 μ g ETR plasmid, 2.5 μ g AP-TGF α plasmid, and 25 μ l of 1 mg per ml PEI solution per 10-cm culture dish). After a 1-day culture, the transfected cells were harvested by trypsinization, washed, and resuspended in 30 ml of Hank's Balanced Salt Solution (HBSS) containing 5 mM HEPES (pH 7.4). The cell suspension was seeded in a 96-well plate (cell plate) at a volume of 80 μ l per well and incubated for 30 min in a CO₂ incubator. For the measurement of antagonist activity, IRL2500 was diluted in 0.01% bovine serum albumin (BSA) and HEPES-containing HBSS (assay buffer) and added to the cell plate at a volume of 10 μ l per well. After 5 min, ET-1, at a final concentration of 0.5 nM, was added to the cell plate at a volume of 10 μ l per well. For the measurement of agonistic activity, after adding 10 μ l of the assay buffer, serially diluted ET-1 was mixed with the cells at a volume of 10 μ l per well. After a 1 h incubation in the CO₂ incubator, aliquots of the conditioned media (80 μ l) were transferred to an empty 96-well plate (conditioned media (CM) plate). Similarly, for the measurement of inverse agonist activity, the cells were mixed with 10 μ l of the assay buffer, followed by the addition of serially diluted IRL2500, and incubated for 4 h before the transfer of the conditioned media. The AP reaction solution (10 mM *p*-nitrophenylphosphate (*p*-NPP), 120 mM Tris-HCl (pH 9.5), 40 mM NaCl, and 10 mM MgCl₂) was dispensed into the cell plates and the CM plates (80 μ l per well). The absorbance at 405 nm (Abs₄₀₅) of the plates was measured, using a microplate reader (SpectraMax 340 PC384, Molecular Devices), before and after a 1 h incubation at room

temperature. AP-TGF α release was calculated as described previously²². The AP-TGF α release signals were fitted to a four-parameter sigmoidal concentration-response curve, using the Prism 7 software (GraphPad Prism), and the pEC₅₀ (equal to $-\log_{10} \text{EC}_{50}$) and E_{max} values were obtained.

To obtain equilibrium dissociation constant (K_B), for each experiment performed in parallel, IC₅₀ values (IRL2500, K-8794, BQ-788), an EC₅₀ value (ET-1), a Hill slope (K , ET-1), and tested concentration of ET-1 (A ; 0.5 nM) were processed as follows⁴⁶:

$$K_B = \frac{\text{IC}_{50}}{1 + \left(\frac{A}{\text{EC}_{50}}\right)^K}$$

The resulting K_B values were logarithmically transformed and their negative values ($\text{p}K_B$) were used to calculate a difference in $\text{p}K_B$ value ($\Delta\text{p}K_B$) for a mutant (MT) receptor as follows by using $\text{p}K_B$ value for WT receptor performed in parallel:

$$\Delta\text{p}K_B = \text{p}K_{B(\text{MT})} - \text{p}K_{B(\text{WT})}$$

The $\text{p}K_B$ and the $\Delta\text{p}K_B$ values were used to calculate mean and SEM.

To measure the constitutive activity in a plasmid volume-dependent manner, HEK293 cells were seeded in a 96-well plate at a concentration of 4×10^5 cells per ml in Opti-MEM I Reduced Serum Media (Thermo Fisher Scientific), in a volume of 80 μ l per well. A transfection mixture was prepared by mixing the PEI transfection reagent (0.2 μ l per well) and plasmids (20 ng AP-TGF α plasmid, titrated ETR plasmid, and an empty vector to balance the total plasmid volume) in Opti-MEM I Reduced Serum Media (20 μ l). The mixture was added to the cells, which were then incubated for 24 h before the transfer of the conditioned media. After adding the AP reaction solution, the absorbances of the cells and the CM plates were measured at 20 min intervals. The AP-TGF α release signals were calculated as described above, and the signal in the mock-transfected conditions was set at the baseline. A glutamine mutation was introduced into the internal FLAG epitope-tagged ET_B and the ET_A constructs at L192^{3,43} and L176^{3,43}, respectively.

Reporting summary. Further information on research design is available in the Nature Research Reporting Summary linked to this article.

Data availability

Coordinates and structure factors have been deposited in the Protein Data Bank, under the accession number 6K1Q for the IRL2500-bound structure. The raw X-ray diffraction images are also available at Zenodo (<https://zenodo.org/record/2803553>). All other data are available from the authors upon reasonable request.

Received: 8 November 2018 Accepted: 21 May 2019

Published online: 21 June 2019

References

- Yanagisawa, M. et al. A novel potent vasoconstrictor peptide produced by vascular endothelial cells. *Nature* **332**, 411–415 (1988).
- Arai, H. et al. Cloning and expression of a cDNA encoding an endothelin receptor. *Nature* **348**, 730–732 (1990).
- Sakurai, T. et al. Cloning of a cDNA encoding a non-isopeptide-selective subtype of the endothelin receptor. *Nature* **348**, 732–735 (1990).
- Channick, R. N. et al. Effects of the dual endothelin-receptor antagonist bosentan in patients with pulmonary hypertension: a randomised placebo-controlled study. *Lancet* **358**, 1119–1123 (2001).
- Rubin, L. J. et al. Bosentan therapy for pulmonary arterial hypertension. *N. Engl. J. Med.* **346**, 896–903 (2002).
- Maguire, J. J. & Davenport, A. P. Endothelin@25—new agonists, antagonists, inhibitors and emerging research frontiers: IUPHAR Review 12. *Br. J. Pharmacol.* **171**, 5555–5572 (2014).
- Davenport, A. P. et al. Endothelin. *Pharmacol. Rev.* **68**, 357–418 (2016).
- Rosano, L., Spinella, F. & Bagnato, A. Endothelin 1 in cancer: biological implications and therapeutic opportunities. *Nat. Rev. Cancer* **13**, 637–651 (2013).
- Clozel, M. et al. Pathophysiological role of endothelin revealed by the first orally active endothelin receptor antagonist. *Nature* **365**, 759–761 (1993).
- Clozel, M. et al. Pharmacological characterization of bosentan, a new potent orally active nonpeptide endothelin receptor antagonist. *J. Pharmacol. Exp. Ther.* **270**, 228–235 (1994).
- Koyama, Y. & Michinaga, S. Regulations of astrocytic functions by endothelins: roles in the pathophysiological responses of damaged brains. *J. Pharmacol. Sci.* **118**, 401–407 (2012).
- Hammond, T. R. et al. Endothelin-B receptor activation in astrocytes regulates the rate of oligodendrocyte regeneration during remyelination. *Cell Rep.* **13**, 2090–2097 (2015).

13. Moldes, O. et al. Neuroprotection afforded by antagonists of endothelin-1 receptors in experimental stroke. *Neuropharmacology* **63**, 1279–1285 (2012).
14. Michinaga, S. et al. Amelioration of cold injury-induced cortical brain edema formation by selective endothelin ET_B receptor antagonists in mice. *PLoS ONE* **9**, e102009 (2014).
15. Michinaga, S. et al. Improvement of cold injury-induced mouse brain edema by endothelin ET_B antagonists is accompanied by decreases in matrixmetalloproteinase 9 and vascular endothelial growth factor-A. *Eur. J. Neurosci.* **42**, 2356–2370 (2015).
16. Michinaga, S. et al. Delayed administration of BQ788, an ET_B antagonist, after experimental traumatic brain injury promotes recovery of blood–brain barrier function and a reduction of cerebral edema in mice. *J. Neurotrauma* **35**, 1481–1494 (2018).
17. Palmer, M. J. 5 Endothelin receptor antagonists: status and learning 20 years on. *Prog. Med. Chem.* **47**, 203–237 (2009).
18. Mucke, H. A. M. Small-molecule endothelin receptor antagonists: a review of patenting activity across therapeutic areas. *IDrugs* **12**, 366–375 (2009).
19. Früh, Th. et al. IRL 2500: a potent ET-B selective endothelin antagonist. *Bioorg. Med. Chem. Lett.* **6**, 2323–2328 (1996).
20. Balwierzczak, J. L. et al. Characterization of a potent and selective endothelin-B receptor antagonist, IRL 2500. *J. Cardiovasc. Pharmacol.* **26**, S393–S396 (1995).
21. Shihoya, W. et al. Activation mechanism of endothelin ET_B receptor by endothelin-1. *Nature* **537**, 363–368 (2016).
22. Shihoya, W. et al. X-ray structures of endothelin ET_B receptor bound to clinical antagonist bosentan and its analog. *Nat. Struct. Mol. Biol.* **24**, 758–764 (2017).
23. Okuta, A., Tani, K., Nishimura, S., Fujiyoshi, Y. & Doi, T. Thermostabilization of the human endothelin type B receptor. *J. Mol. Biol.* **428**, 2265–2274 (2016).
24. Inoue, A. et al. TGF α shedding assay: an accurate and versatile method for detecting GPCR activation. *Nat. Methods* **9**, 1021–1029 (2012).
25. Thorsen, T. S., Matt, R., Weis, W. I. & Kobilka, B. K. Modified T4 lysozyme fusion proteins facilitate G protein-coupled receptor crystallogenesis. *Structure* **22**, 1657–1664 (2014).
26. Caffrey, M. & Cherezov, V. Crystallizing membrane proteins using lipidic mesophases. *Nat. Protoc.* **4**, 706–731 (2009).
27. Yamashita, K., Hirata, K. & Yamamoto, M. KAMO: towards automated data processing for microcrystals. *Acta Crystallogr. D Struct. Biol.* **74**, 441–449 (2018).
28. Ballesteros, J. A. & Weinstein, H. [19] Integrated methods for the construction of three-dimensional models and computational probing of structure-function relations in G protein-coupled receptors. *Methods Neurosci.* **25**, 366–428 (1995).
29. Sakaki, J. et al. Discovery of IRL 3461: a novel and potent endothelin antagonist with balanced ETA/ETB affinity. *Bioorg. Med. Chem. Lett.* **8**, 2241–2246 (1998).
30. Soudijn, W., van Wijngaarden, I. & Ijzerman, A. P. Structure–activity relationships of inverse agonists for G-protein-coupled receptors. *Med. Res. Rev.* **25**, 398–426 (2005).
31. Trülsch, B. et al. Detection of thyroid-stimulating hormone receptor and G α mutations: in 75 toxic thyroid nodules by denaturing gradient gel electrophoresis. *J. Mol. Med.* **78**, 684–691 (2001).
32. Moore, A. R. et al. Recurrent activating mutations of G-protein-coupled receptor CYSLTR2 in uveal melanoma. *Nat. Genet.* **48**, 675–680 (2016).
33. Ishikawa, K. et al. Biochemical and pharmacological profile of a potent and selective endothelin B-receptor antagonist, BQ-788. *Proc. Natl Acad. Sci. USA* **91**, 4892–4896 (1994).
34. Peng, Y. et al. 5-HT_{2C} receptor structures reveal the structural basis of GPCR polypharmacology. *Cell* **172**, 719–730 (2018).
35. Katritch, V. et al. Allosteric sodium in class A GPCR signaling. *Trends Biochem. Sci.* **39**, 233–244 (2014).
36. Hori, T. et al. Na⁺-mimicking ligands stabilize the inactive state of leukotriene B₄ receptor BLT₁. *Nat. Chem. Biol.* **14**, 262–269 (2018).
37. Shihoya, W. et al. Crystal structures of human ETB receptor provide mechanistic insight into receptor activation and partial activation. *Nat. Commun.* **9**, 4711 (2018).
38. Hirata, K. et al. ZOO: an automatic data-collection system for high-throughput structure analysis in protein microcrystallography. *Acta Crystallogr. D Biol. Crystallogr.* **75**, 138–150 (2019).
39. Ueno, G. et al. Remote access and automation of SPring-8 MX beamlines. *AIP Conf. Proc.* **1741**, 050021 (2016).
40. Yamashita, K., Hirata, K. & Yamamoto, M. KAMO: towards automated data processing for microcrystals. *Acta Crystallogr. D Biol. Crystallogr.* **74**, 441–449 (2018).
41. Kabsch, W. XDS. *Acta Crystallogr. D Biol. Crystallogr.* **66**, 125–132 (2010).
42. McCoy, A. J. et al. Phaser crystallographic software. *J. Appl. Crystallogr.* **40**, 658–674 (2007).
43. Emsley, P., Lohkamp, B., Scott, W. G. & Cowtan, K. Features and development of Coot. *Acta Crystallogr. D Biol. Crystallogr.* **66**, 486–501 (2010).
44. Adams, P. D. et al. PHENIX: a comprehensive Python-based system for macromolecular structure solution. *Acta Crystallogr. D Biol. Crystallogr.* **66**, 213–221 (2010).
45. Chen, V. B. et al. MolProbity: all-atom structure validation for macromolecular crystallography. *Acta Crystallogr. D Biol. Crystallogr.* **66**, 12–21 (2010).
46. Cheng, H. C. The power issue: determination of K-B or K-i from IC₅₀—a closer look at the Cheng-Prusoff equation, the Schild plot and related power equations. *J. Pharmacol. Toxicol. Methods* **46**, 61–71 (2001).

Acknowledgements

The diffraction experiments were performed at SPring-8 BL32XU (proposal 2017A2527 and 2017B2578). The authors thank the beamline staff at BL32XU of SPring-8 (Sayo, Japan) for technical assistance during data collection. The authors also thank Kouki Kawakami, Takeaki Shibata, and Ayumi Inoue (Tohoku University, Japan) for technical assistance in the characterization of the L³43Q-mutant ET_B and ET_A receptors. The authors also thank K. Yamashita for the assistance of the PDB deposition and uploading the raw data. This work was supported by grants from the Platform for Drug Discovery, Informatics and Structural Life Science by the Ministry of Education, Culture, Sports, Science and Technology (MEXT), JSPS KAKENHI grants 16H06294 (O.N.), 17J30010 (W.S.), 30809421 (W.S.), 17K08264 (A.I.), and the Japan Agency for Medical Research and Development (AMED) grants: the PRIME JP17gm5910013 (A.I.) and the LEAP JP17gm0010004 (A.I. and J.A.), and the National Institute of Biomedical Innovation.

Author contributions

C.N. expressed, purified, and crystallized the IRL2500-bound ET_B receptor, collected data, and refined the structures. W.S. designed all of the experiments, initially crystallized the receptor, and refined the structure. A.I., F.M.N.K. and J.A. performed and oversaw the cell-based assays. The manuscript was prepared by C.N., W.S., A.I., and O.N. W.S. and O.N. supervised the research.


Additional information

Supplementary information accompanies this paper at <https://doi.org/10.1038/s42003-019-0482-7>.

Competing interests: The authors declare no competing interests.

Reprints and permission information is available online at <http://npg.nature.com/reprintsandpermissions/>

Publisher's note: Springer Nature remains neutral with regard to jurisdictional claims in published maps and institutional affiliations.

 **Open Access** This article is licensed under a Creative Commons Attribution 4.0 International License, which permits use, sharing, adaptation, distribution and reproduction in any medium or format, as long as you give appropriate credit to the original author(s) and the source, provide a link to the Creative Commons license, and indicate if changes were made. The images or other third party material in this article are included in the article's Creative Commons license, unless indicated otherwise in a credit line to the material. If material is not included in the article's Creative Commons license and your intended use is not permitted by statutory regulation or exceeds the permitted use, you will need to obtain permission directly from the copyright holder. To view a copy of this license, visit <http://creativecommons.org/licenses/by/4.0/>.

© The Author(s) 2019